



**HAL**  
open science

## A step toward calculating the uncertainties in combined GIXRF-XRR

Stéphanie Melhem, Yves Ménesguen, Emmanuel Nolot, Marie-Christine Lépy

► **To cite this version:**

Stéphanie Melhem, Yves Ménesguen, Emmanuel Nolot, Marie-Christine Lépy. A step toward calculating the uncertainties in combined GIXRF-XRR. *X-Ray Spectrometry*, 2023, 52, pp.412-422. 10.1002/xrs.3377 . cea-04563756

**HAL Id: cea-04563756**

**<https://cea.hal.science/cea-04563756v1>**

Submitted on 30 Apr 2024

**HAL** is a multi-disciplinary open access archive for the deposit and dissemination of scientific research documents, whether they are published or not. The documents may come from teaching and research institutions in France or abroad, or from public or private research centers.

L'archive ouverte pluridisciplinaire **HAL**, est destinée au dépôt et à la diffusion de documents scientifiques de niveau recherche, publiés ou non, émanant des établissements d'enseignement et de recherche français ou étrangers, des laboratoires publics ou privés.



Distributed under a Creative Commons Attribution - NonCommercial - NoDerivatives 4.0  
International License

# A step toward calculating the uncertainties in combined GIXRF-XRR

Stephanie Melhem<sup>1</sup>  | Yves Ménesguen<sup>1</sup>  | Emmanuel Nolot<sup>2</sup> | Marie-Christine Lépy<sup>1</sup>

<sup>1</sup>Université Paris-Saclay, CEA, LIST, Laboratoire National Henri Becquerel (LNE-LNHB), Palaiseau, France

<sup>2</sup>CEA, LETI, Grenoble, France

## Correspondence

Stephanie Melhem, Université Paris-Saclay, CEA, LIST, Laboratoire National Henri Becquerel (LNE-LNHB), F-91120 Palaiseau, France.

Email: [stephanie.melhem@cea.fr](mailto:stephanie.melhem@cea.fr)

## Abstract

The combination of X-ray reflectivity (XRR) and grazing incidence X-ray fluorescence (GIXRF) is a surface sensitive analytical method, which can be used for the characterization of thin films and multilayered materials. Both of these techniques are implemented on the same experimental setup and make use of similar mechanical processes and the same fundamental physical concept required for a combined data analysis. The combination of these techniques removes ambiguous results for the characterization of nanometer layers, as well as nanometer depth profiles, resulting in more accurate characterization of thickness, roughness, density, and elemental composition. Due to the vast number of fitting parameters, the estimation of the thin film sample structure is a challenging task. In this paper, we propose a recursive method for estimating the uncertainties of data from GIXRF-XRR analysis, based on a Bootstrap statistical method. This approach relies on re-sampling a dataset to estimate statistics on a population by applying random weights. We applied this method on an as-deposited chalcogenide germanium, antimony, and tellurium (GST) thin film with a carbon-capping layer. We found good agreement between the experimental and the theoretical XRR-GIXRF values for a sample structure model, of which the parameters were determined within a confidence interval using the bootstrap method. We also propose an approach for calculating the uncertainty on the solid angle of detection based on Monte Carlo simulations.

## KEYWORDS

grazing incidence X-ray fluorescence, metrology, X-ray reflectivity

## 1 | INTRODUCTION

Telluride-based chalcogenide thin films are being widely used in data storage devices.<sup>1</sup> These materials such as GeTe, SbTe, GeSbTe, are characterized by their phase

change properties from amorphous to crystalline, that have led recently to their use in non-volatile resistive memories in Phase Change Random Access Memories.<sup>2,3</sup> The phase change properties are obtained by applying heat sources such as optical and/or electrical pulses of

This is an open access article under the terms of the [Creative Commons Attribution-NonCommercial-NoDerivs](https://creativecommons.org/licenses/by-nc-nd/4.0/) License, which permits use and distribution in any medium, provided the original work is properly cited, the use is non-commercial and no modifications or adaptations are made.

© 2023 The Authors. *X-Ray Spectrometry* published by John Wiley & Sons Ltd.

different intensities and durations,<sup>4,5</sup> that modify the chemical structure of the material and therefore, its optical and electrical properties. Furthermore, the crystallization temperature and the optical properties of multilayered GST (germanium, antimony, and tellurium) samples change with their chemical composition and their elemental depth profile.<sup>6,7</sup> In order to study these physical and chemical properties, the characterization of GST multilayered thin-films is required.

Reference-free grazing incidence X-ray fluorescence (GIXRF) in combination with X-ray reflectivity (XRR) is one of the methods used for the characterization of layered thin films in the nanometer range.<sup>8,9</sup> For non-organic materials, GIXRF is a powerful non-destructive technique that can be used for elemental depth profiling, as well as for determination of thickness, density, and roughness of thin films. This technique was formalized by De Boer and it is based on the intensity changes of X-ray standing waves (XSW) created by the interference between the incident and the reflected X-ray waves within the thin layers when varying the angle of incidence.<sup>10–12</sup>

X-ray reflectivity is a sensitive analysis technique used for the characterization of thin film surfaces and interfaces, based on the measurement of the reflected intensity by varying the angle of incidence in the grazing range. This method is used to determine the density, interface roughness and thickness of thin layers ranging from a few nanometers to some hundred nanometers—as well as the optical properties of the reflecting interfaces.<sup>13</sup>

Combining these two methods results in better characterization of quantitative chemical depth-dependence in thin films. In addition, most X-ray fluorescence (XRF) quantification techniques depend on reference materials or calibration standards, both of which are difficult to obtain for a wide range of materials.<sup>14</sup> To circumvent this problem, reference-free GIXRF is used,<sup>15</sup> relying on the use of calibrated instrumentation<sup>16,17</sup> and the knowledge of the fundamental atomic parameters of the elements, rather than on the use of suitable reference materials with similar characteristics to the sample to be analyzed.<sup>15</sup>

A key step in validating the reference-free GIXRF-XRR analysis method is to determine the parameter uncertainties. This is a challenging task due to the large number of optimization parameters. In this paper, we propose a method to determine the confidence intervals linked to reference-free GIXRF-XRR analysis implemented in the goniometer CASTOR (*chambre d'analyse spectrométrique par réflexion ou transmission*)<sup>18</sup> at the SOLEIL synchrotron by using a Bootstrap sampling method. In addition, we calculate the uncertainty of the

solid angle of XRF detection analysis following the recommendations in the Guide to the Expression of Uncertainty in measurement (GUM)<sup>19,20</sup> using Monte Carlo simulations.<sup>21</sup>

## 2 | EXPERIMENTAL

### 2.1 | Sample preparation

The sample was prepared by CEA LETI by depositing 50 nm-thick chalcogenide material on 300  $\mu\text{m}$  silicon (001) wafers using magnetron sputtering of a  $\text{Ge}_2\text{Sb}_2\text{Te}_5$  alloyed target (Applied Materials Endura<sup>®</sup> Clover<sup>™</sup> multi-cathode PVD chamber). The deposition temperature was kept close to 60°C for all samples and the chamber base pressure was  $1.33 \times 10^{-4}$  Pa.<sup>22</sup> The chalcogenide material was capped in situ with a 3.5 nm-thick amorphous carbon layer deposited in pulse-DC mode in order to prevent aging.<sup>23</sup>

### 2.2 | Instrumentation

The reference-free GIXRF-XRR measurements were conducted with the goniometer CASTOR<sup>18</sup> on the METROLOGIE beamline at the SOLEIL synchrotron.<sup>24</sup> The irradiation chamber was developed by *Laboratoire National Henri Becquerel* (CEA/LNE-LNHB), based on the model of the Physikalisch-Technische Bundesanstalt (PTB, Germany) and the Technical University of Berlin.<sup>25,26</sup> A 3D drawing of the chamber is shown in Figure 1. The instrument is installed on the “hard X-ray” branch equipped with a double Si (111) crystal monochromator with a Bragg angular range able to select an energy between 3 and 45 keV.

The irradiation chamber encloses a seven-axis manipulator, including four translation axes and three rotation axes. Among these axes, five are used to control the sample position ( $T_z$ ,  $T_s$ ,  $T_x$ ,  $R_x$ , and  $R_{01}$ ) and two for the detection arm position ( $T_{z2}$  and  $R_{02}$ ) as shown in Figure 1. The rotation axes ( $R_{01}$  and  $R_{02}$ ) are the critical ones, since they can move freely to adjust the incident angle on the sample, as well as the detection angle. The XRR measurements were taken in  $\theta/2\theta$  configuration using an AXUV photodiode (IRD Optodiode) placed on the  $R_{02}$  arm. The XRF signal was acquired with an energy-dispersive spectrometer (EDS) (Silicon Drift Detector (SDD) from Amptek) placed at 90° from the excitation beam and at a distance of 13 mm from the sample surface. Figure 2 shows the geometry setup for reference-free XRR-GIXRF measurements.

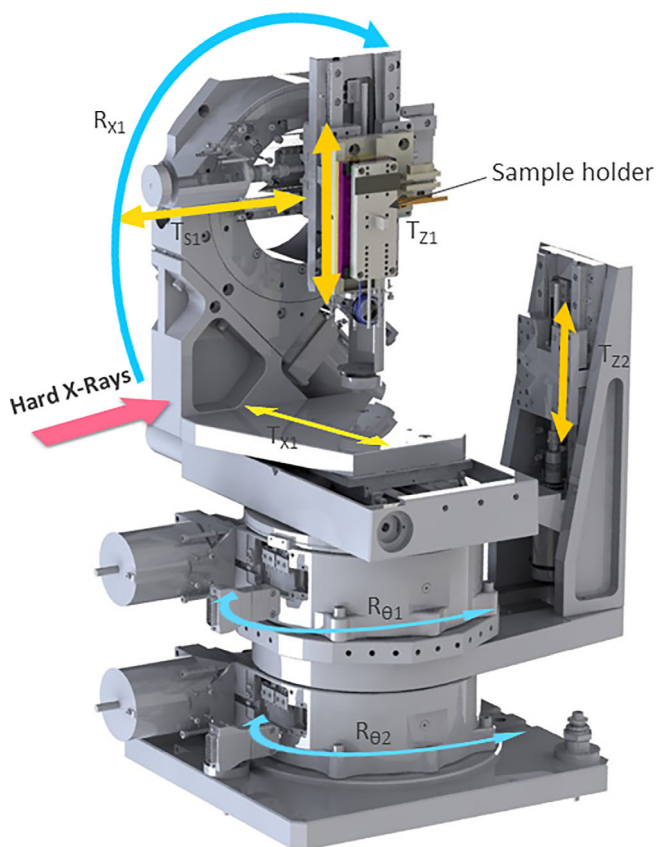


FIGURE 1 3D drawing representing the goniometer CASTOR with the axes of motion.

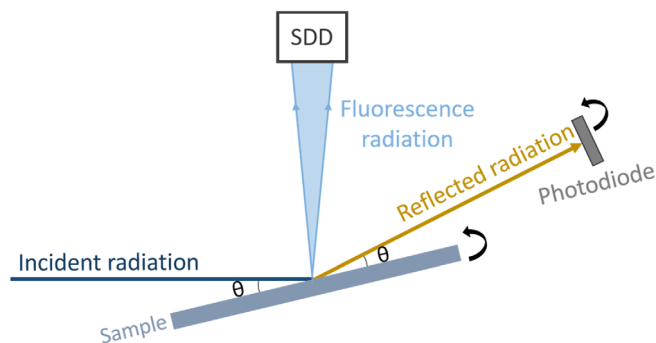


FIGURE 2 Geometry setup for reference free XRR-GIXRF measurements, composed of an energy dispersive spectrometer to record the fluorescence and a photodiode to measure the reflectivity while varying the incident angle. SDD, silicon drift detector.

### 3 | SIMULATION AND OPTIMIZATION

Reference-free GIXRF-XRR analysis is based on the knowledge of the fundamental atomic parameters and the instrumental parameters, such as the intensity of the excitation radiation, the beam geometry and the solid angle of detection. In this section, we provide a short

description of the simulations and fitting procedures for XRR-GIXRF data, followed by the solid angle calculation method.

First, the data of XRR and GIXRF were acquired using LabVIEW. Afterwards, we performed the combined analysis of XRR-GIXRF using several software packages:

1. XRR data were analyzed with IMD<sup>27</sup> to obtain an estimation of the structural composition,
2. GIXRF spectra were fitted with COLEGRAM<sup>28</sup> to derive the intensity of the fluorescence X-ray lines, and finally
3. GIXRF-XRR analysis was performed using in-house software called ELIXIR to derive the sample structure and the associated uncertainties based on the model obtained with IMD and the fitted fluorescence data.

#### 3.1 | Combined GIXRF-XRR

GIXRF-XRR method is based on measuring and analyzing the unique angular dependent fluorescence emissions resulting from the interaction of specific atoms with the XSW, while varying the angle of incidence.

The reflectivity of X-rays that occurs at the interfaces of multilayers can be calculated using Parratt's recursive method<sup>29</sup> with the Névoat–Croce formalism to take into account the roughness<sup>30</sup> by computing the electromagnetic field as a function of the incidence angle ( $\theta$ ) based on reflection and refraction at the interfaces as:

$$XRR(\theta) = \|E_r(0, \theta) + E_t(0, \theta)\|^2. \quad (1)$$

At grazing incidence angles, the reflected part of the incident beam interferes with the incoming beam forming standing waves, within the limits of coherence, standing waves above the surface and within the first tenths of a nanometer inside the material. The generated X-ray standing wave inside the thin layers enhances the probability of ionizing an element present at its antinodes, which makes it a very sensitive probe for determining depth profiles of elements and interfacial roughness<sup>31</sup> since it depends on the incident angle and the photon energy. In addition, GIXRF uses XRF incident angle dependency, especially below the substrate's critical angle, where variations of XSW intensity affect the angular intensity profile. Due to the change of the penetration depth and the interference of incident and reflected fields when varying the incident angle, the GIXRF spectrum shows variations in the fluorescence intensity related to the elemental depth distribution in the sample. The emitted fluorescence is calculated using the same recursive formalism of Parratt. This approach is based on the

calculation of the derivative of the Poynting vector as developed by De Boer<sup>10</sup> through the calculation of the reflection and transmission coefficients at each layer. The detected fluorescence is computed by taking into account the variation of the field and the interface roughnesses by cutting the layers into thin slabs<sup>32</sup> as

$$\begin{aligned} XRF_i = & \Omega(\theta) I_0 T \eta_i \tau_i \omega_i \cdot \sum_j W_i(z_j) \rho(z_j) (z_j - z_{j-1}) \\ & \cdot ||E_r(z_j, \theta) + E_t(z_j, \theta)|| \\ & \exp\left(-\sum_{h=1}^{j-1} \mu_j(z_h) \rho(z_h) (z_h - z_{h-1})\right), \end{aligned} \quad (2)$$

where,  $\Omega(\theta)$ : the solid angle of detection,  $T$ : the acquisition live time of each spectrum,  $I_0$ : the flux of incident photons,  $\eta_i$ : the detector full-energy peak efficiency at the line energy of element  $i$ ,  $\tau_i$ : the photoelectric cross section of element  $i$  at incoming energy,  $\omega_i$ : the partial fluorescence yield of element  $i$ ,  $W_i(z_j)$ : the weight fraction of element  $i$  at depth  $z_j$ ,  $\rho(z_j)$ : the density at the same depth  $z_j$ ,  $\mu_j(z_h)$ : the attenuation coefficient to take into account the reabsorption of the emitted fluorescence when passing through the upper layers,  $E_r(z_j, \theta)$  and  $E_t(z_j, \theta)$ : the transmitted and the reflected electric fields.

As initial settings for the optimization technique, the experimental setup parameters and the sample parameters (roughnesses, thicknesses, densities, and elemental compositions), must be defined. The simulated GIXRF and XRR data for each parameter are then computed.

The optimization procedure should consider the different dynamic ranges of the XRR and the GIXRF responses. The XRR is normalized to the incident photon flux exhibiting a signal ranging from 0 to 1, with features that extend over several logarithmic orders of magnitude. On the other hand, the GIXRF curves present peak areas ranging from hundreds to millions of counts. Consequently, employing the same  $\chi^2$  function for both techniques in the optimization procedure may prove challenging, as one experimental curve may dominate over the other.

Afterwards, calculated GIXRF-XRR data are fitted to the experimental data with ELIXIR by adjusting the model parameters using two  $\chi^2$  cost functions. For the reflectivity, the data are multiplied by the incident angle to the power of 5 to simplify fitting and amplify the effect of tiny density fluctuations on the fit for the reflectivity as:

$$Cost_{XRR} = \sum_{i=1}^n \frac{(\theta_i^5 \cdot e^{XRR_{i,Th}} - \theta_i^5 \cdot e^{XRR_{i,Exp}})^2}{\theta_i^5 \cdot e^{XRR_{i,Th}}}, \quad (3)$$

and for the fluorescence the cost function is calculated as:

$$Cost_{XRF} = \sum_{i=1}^n \frac{(XRF_{i,Th} - XRF_{i,Exp})^2}{XRF_{i,Th}} \cdot \frac{1}{\text{Max}(XRF_{Th})}. \quad (4)$$

In these equations,  $n$  is the number of angular steps,  $\text{Max}(XRF_{Th})$  is the maximum calculated value of the XRF curve,  $XRR_{i,Th}$ ,  $XRR_{i,Exp}$ ,  $XRF_{i,Th}$ , and  $XRF_{i,Exp}$  are the theoretical and the experimental values for the reflectivity and the fluorescence at each angle. Finally, once the stopping criteria are reached, the best parameter set is obtained.

### 3.2 | Solid angle

The solid angle of detection of the energy-dispersive spectrometer is an important parameter influencing the efficiency of the X-ray signal measurement. Thus, in order to model correctly the sample in the fitting procedure, some geometrical aspects must be accurately taken into account. These include the footprint of the incoming beam on the sample and the solid angle of detection.

The shape and the size of the incoming beam on the sample is defined by a slit placed at 1 m ahead, vertically to limit the horizontal divergence on the sample. The use of a rectangular slit results in a rectangular-shaped beam impinging upon the sample. The footprint width is 0.3 mm corresponds to the slit vertical width and its length is defined as:

$$L = \frac{S_h}{\sin \theta}, \quad (5)$$

where  $S_h$  represents the slit horizontal width. The incident flux can be adjusted by changing the height of the slit (up to 3 mm in height). In addition, other factors impact the solid angle of detection, such as the sample alignment and the geometrical characteristics of the detector, as illustrated in Figure 3.

Therefore, the solid angle as a function of the incidence angle is calculated as:

$$\Omega(\theta) = \frac{1}{A_s} \iint_{A_s} \Omega_r(r) dx dy, \quad (6)$$

where  $A_s$  is the beam footprint on the sample surface detected by the SDD, calculated as a function of the incidence angle, the slit dimensions and the samples length and  $\Omega_r(r)$  is the solid angle as a function of the radial distance expressed as:

$$\Omega_r(r) = \int^{S(r)} \int \frac{\sin(\beta)}{(d_1 + e + d_2)^2 + (r+x)^2 + y^2} dx dy. \quad (7)$$

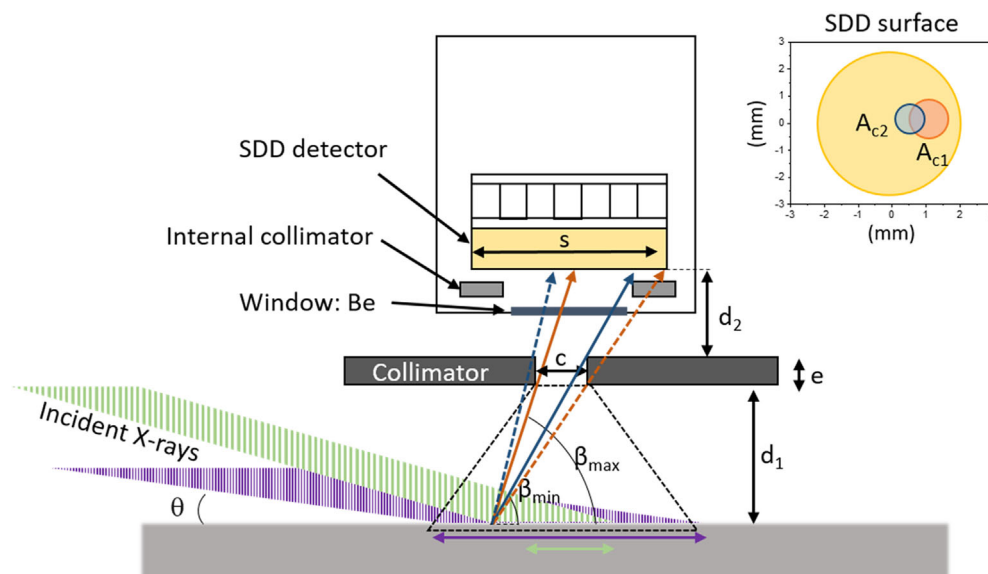


**FIGURE 3** Schematic showing the geometric parameters of the EDS that affect the solid angle of detection.  $e$  and  $c$  are the thickness and the aperture of the collimator,  $d_1$  is the distance between the sample and the collimator,  $d_2$  is the distance between the collimator and the SDD surface, and  $s$  is the diameter of the SDD. The lines correspond to the front (orange) and back (blue) sides of the collimator and the dashed lines represent the rays that do not pass through the front (orange) and back (blue) sides of collimator. EDS, energy-dispersive spectrometer; SDD, silicon drift detector.

$e$  and  $c$  represent the thickness and the aperture of the collimator respectively,  $d_1$  represents the distance between the sample and the collimator,  $d_2$  is the distance between the collimator and the SDD silicon chip,  $s$  is the diameter of the SDD, and  $l_E$  is the length of the sample.

The angle  $\beta$  is calculated as:

$$\beta = \arctan \frac{d_1 + e + d_2}{\sqrt{(r+x)^2 + y^2}}, \quad (8)$$

and the integral limit  $S(r)$  is represented as the common region between the SDD active area  $A_{SDD}$  and the projected areas on the SDD surface of the front and back sides of the collimator respectively,  $A_{c1}$  and  $A_{c2}$ .<sup>32</sup>

## 4 | UNCERTAINTY CALCULATION METHODS OF COMBINED XRR-GIXRF ANALYSIS

### 4.1 | Solid angle uncertainty

The objective of this section is to present a systematic method for the uncertainty calculation of the solid angle of detection. In the GIXRF measurements, the solid angle is dependent on several parameters including the accuracy of the sample alignment, the uncertainty on the footprint position and the uncertainties related to the geometrical factors of the SDD.

A proper beam alignment in GIXRF-XRR is crucial to ensure the quality and the reproducibility of the GIXRF-XRR measurements. It maximizes the signal-to-noise ratio and ensure that accurate and reliable results are obtained. The alignment procedure of CASTOR requires iterative steps that consist of first aligning the rotating axis with the beam axis and then aligning the sample with the beam.

The uncertainty on the sample alignment includes the uncertainty of repeatability, the resolution and the precision of the translation and rotation stages. The rotation stages in the goniometer are encoded with a Renishaw linear rule with an accuracy of 0.0003 degrees and a minimum pitch of 0.002 degrees resulting in a combined uncertainty on the position of the rotation axis of 0.0005 degrees. Meanwhile, the minimum increment size for the translation axis is 0.02 mm, leading to a positional uncertainty of 0.004 mm following the GUM.

In addition, the uncertainty of the footprint position is related to the slit dimensions and the angle of incidence. To include this uncertainty in the calculation of the solid angle of detection, we must consider the uncertainties of the slit dimensions as well as the uncertainties of the rotation axes.

To calculate the uncertainties on the solid angle of detection, one must take into account the uncertainties on all the geometrical parameters ( $d_1, d_2, e, c, s$ ),<sup>19,20</sup> the uncertainty on the slit dimensions and the uncertainties on the rotation stages which affect the solid angle.

However, in this current work, we have chosen to focus on the uncertainty associated with the geometrical factors of the detector, and have not taken into account the uncertainties on the other parameters mentioned.

This procedure can be performed by selecting the most appropriate probability density function (PDF) for each of the input quantities, then applying an estimated uncertainty, followed by Monte Carlo simulations to generate random values of each parameter (assuming either a Gaussian or a uniform distribution as  $X = (X_{min}, X_{max})$  in which  $X_{min}$  and  $X_{max}$  represent the lower and upper limit values of each parameter).

First, the distance  $d_1$  ( $\sim 13$  mm) between the collimator and the samples is modeled using a uniform probability distribution, since the associated uncertainty is attributed to the resolution of the detector translation stage of 0.1 mm. Thus, the uncertainty of this parameter is calculated following the (GUM) as:

$$U_i = \frac{a_i}{2\sqrt{3}} \quad (9)$$

where  $a_i$  is the resolution of the translation stage of the SDD.

The aperture of the collimator  $c$  is measured with an uncertainty of  $2\ \mu\text{m}$  using a Quick Scope manual vision machine. The uncertainty of the collimator thickness  $e$  is calculated by performing a series of repeated measurements using a Roch height gauge and taking into account the calibration uncertainty. The nominal values of  $d_2$  and  $s$  were provided by the SDD manufacturer. For these parameters, their distribution function is unknown, thus the description of the uncertainty is typically assumed to be a joint multi-variable normal distribution around the nominal values. To help illustrate the point, these parameters were assigned an estimated uncertainty of 0.1 mm given by the manufacturer. The geometrical parameters with their uncertainties and their probability density functions are given in Table 1.

After all the input parameters have been defined with their uncertainties, Monte Carlo simulations are performed for each of them to calculate the output uncertainties of the system. Its principle is to resample the inputs (i.e., geometrical parameters) in large number and use them to propagate the uncertainties to the output (i.e., solid angle).<sup>33</sup> For this method, 100 simulations were applied to generate new samples for each parameter and therefore,  $n$  new samples of the solid angle as a function of the incident angle. In this case, we can calculate the type A uncertainty on the solid angle (uncertainty due to the repeatability) at each incident angle using this equation:

TABLE 1 Geometrical parameters with their uncertainties, and probability distribution functions.

Parameter name	Geometrical parameter	Value (mm)	Probability distribution function
Sample-collimator distance	$d_1$	$13.00 \pm 0.03$	Uniform
Collimator-SDD distance	$d_2$	$2.33 \pm 0.10$	Normal
Collimator thickness	$e$	$2.071 \pm 0.004$	Normal
Collimator diameter	$c$	$1.971 \pm 0.002$	Normal
SDD diameter	$s$	$4.66 \pm 0.10$	Normal

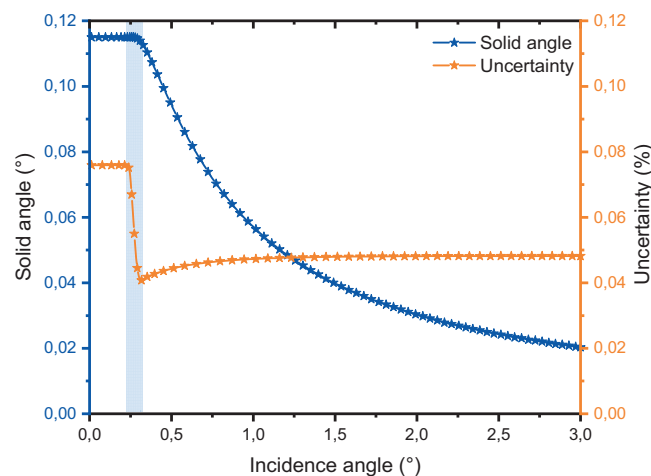


FIGURE 4 Solid angle (blue) with associated partial uncertainty (orange) at each incidence angle taking into account the uncertainties on the geometrical parameters.

$$U(\theta) = \frac{\sigma_i(\theta)}{\sqrt{n}}, \quad (10)$$

where  $n$  is the size of the population and  $\sigma_i(\theta)$  is the standard deviation.

Figure 4 shows the results of the calculation of the solid angle (blue curve) with its associated uncertainty (orange curve) as function of the incident angle. At low incident angles ( $0-0.25^\circ$ ), the solid angle is constant and relatively high due to the beam spot on the sample being larger than the field of view of the SDD with its collimator. By increasing the incident angle, the slope of the curve becomes steep as the solid angle becomes very low due to the decrease of the beam size on the sample.

Application of Monte Carlo simulations produces a low relative uncertainty on solid angles due to the low uncertainties on the dimensions of the detector components. We notice a drop in the relative uncertainty in the hatched region of the solid angle to 0.04 % at 0.3°. This decrease is related to the lower impact of  $d_1$  on the solid angle in this angular region. In fact, at higher angles, the beam footprint is completely included in the field of view of the SDD detector. At higher incident angles, the uncertainty remains approximately constant.

## 4.2 | XRR-GIXRF uncertainty calculation using random weight Bootstrap

The random weight Bootstrap method was introduced by Efron<sup>34</sup> to obtain statistical information including standard uncertainties, confidence intervals and hypothesis tests without any prior knowledge about the probability distributions. The principle of the Bootstrap method is based on Monte Carlo simulations to create many simulated data at low cost by resampling one single dataset, thus allowing information to be collected on the sample statistics without any repetition of the measurements.<sup>35</sup> The generation of Bootstrap samples can be achieved by applying random integer weights indicating the number of times each data is repeated in the resampling.

While repeating the measurements of XRR and GIXRF is time consuming, bootstrapping can be useful to estimate the uncertainties and construct the confidence intervals for the fitting parameters.

In our case, the method of the weight application is different., We will consider that each value of the intensity of XRR and GIXRF for each incidence angle will represent one sample.

As mentioned previously, the fitting procedure to estimate the sample structure is performed using a differential method with the  $\chi^2$  cost functions of the reflectivity and the fluorescence. Thus, to generate new data, a uniform weight between 0 and 1 is applied to each angular step for the XRR and the GIXRF data. In this case, the normalized cost function for the XRR is expressed as:

$$Cost_{XRR} = \sum_{i=1}^n B_i \cdot \frac{(\theta_i^5 \cdot e^{XRR_{i,Th}} - \theta_i^5 \cdot e^{XRR_{i,Exp}})^2}{\theta_i^5 \cdot e^{XRR_{i,Th}}}, \quad (11)$$

and the normalized cost function for the GIXRF becomes:

$$Cost_{XRF} = \sum_{i=1}^n B_i \cdot \frac{(XRF_{i,Th} - XRF_{i,Exp})^2}{XRF_{i,Th}} \cdot \frac{1}{\text{Max}(XRF_{Th})}, \quad (12)$$

where  $B_i$  is the applied weight.

By repeating this procedure, we obtain a new set of possible sample structures in which the thicknesses, roughnesses, densities, and compositions vary. We can then calculate the mean, the standard deviation, covariance, etc., and the confidence intervals associated to every fitted parameter. A flowchart of the optimization algorithm of our Bootstrap uncertainty calculation is shown in Figure 5.

## 5 | RESULTS AND DISCUSSION

We performed combined GIXRF-XRR analysis on a multi-layer sample: C (3.5 nm)/Ge<sub>2</sub>Sb<sub>2</sub>Te<sub>5</sub> (50 nm)/Si substrate. The fluorescence spectra were measured at angles from 0 to 3°, with an acquisition time of 30 s using 11.5 keV photon energy in order to excite Ge-K<sub>α,β</sub>, Sb-L<sub>α,β</sub>, and Te-L<sub>α,β</sub> lines. The photon flux at the XRF excitation energy, for a height slit of 0.3 mm is  $2.27 \times 10^8 \text{ s}^{-1}$ . Figure 6 displays the fluorescence spectrum measured with the EDS at the incident angle of 0.5°. The fluorescence peaks of each element were processed with COLEGRAM after selection of different regions of interest (ROI). The fit is based on iterations of a  $\chi^2$  adjustment procedure. Several peaks were fitted in each ROI, using Gaussian profiles, taking into account the variation of the energy resolution: the Gaussian standard deviation ( $\sigma$ ) of several peaks in the same ROI, are linked as:

$$\sigma(E)^2 = \sigma_0^2 + kE, \quad (13)$$

where  $E$  is the energy position,  $\sigma_0$  is the width offset and  $k$  is the slope of the function. These width parameters are common to all peaks characterized by the same “sigma” shape. As presented in the fluorescence spectrum, several peaks were observed, including L emission lines of tellurium and antimony, K lines of sulfur and germanium and the scattering peaks (Compton and Rayleigh). Sulfur is likely present due to the contamination during the sample preparation process. Furthermore, the XRF spectrum exhibits a notable overlap of peaks between the L lines of tellurium (Te) and antimony (Sb) as well as between the K<sub>β</sub> line of Ge and Compton scattering. This peaks overlap is due to the similar or close energies of the overlapping peaks, which cannot be distinguished by the low-resolution of the EDS.

The GIXRF intensities were then obtained by batch processing, which extracts the surface area of each peak for each incident angle.

X-ray reflectivity was measured with an incident energy of 8 keV between 0 and 3°. For XRR, we increased the slit height to the maximum (3 mm) in which we



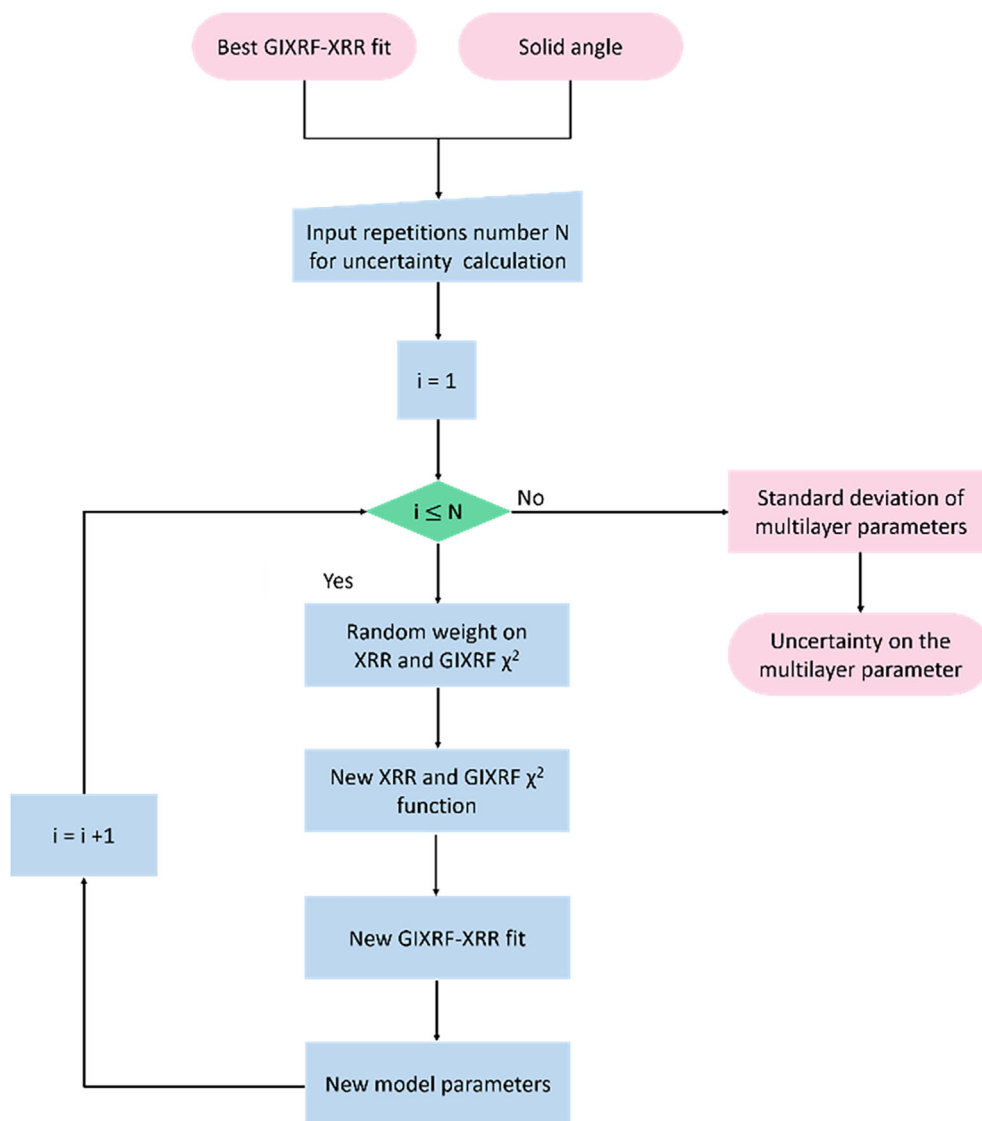


FIGURE 5 Optimization algorithm of bootstrap uncertainty calculation.

obtained a photon flux of  $8.68 \times 10^8 \text{ s}^{-1}$ . The XRR curve is first fitted with IMD to obtain an approximation of the sample structure. This structure is then imported into ELIXIR to perform the combined analysis of GIXRF-XRR. As mentioned above, the best model is estimated by fitting the GIXRF and the XRR simultaneously using the differential algorithm that performs a global minimization search with  $\chi^2$  minimization criterion.

### 5.1 | Analysis of a C-capped GST monolayer

Figures 7 and 8 represent the experimental and simulated data of XRR and GIXRF respectively, collected from a GST sample using ELIXIR. As shown in Figure 7, the fit is in good agreement for the XRR data, showing same critical angle ( $\sim 0.22^\circ$ ), period, number of Kiessig fringes and reflected intensity, giving confidence in the

structural parameters (roughnesses, densities, thicknesses, and elemental composition). Below the critical angle, the difference in the intensity is due to the experimental geometrical factors. The amplitude difference of the Kiessig fringes between the experimental data and the fit is related to the off-specular scattering, which occurs at rough surfaces (i.e., roughness  $\geq \lambda$ ).<sup>36,37</sup>

As shown in Figure 8, below the critical angle, the fluorescence intensity for Ge- $K_\alpha$ , Sb- $L_\alpha$ , and Te- $L_\alpha$  is low due to the total reflection of incident X-rays. The angular-dependent Ge- $K_\alpha$ , Sb- $L_\alpha$ , and Te- $L_\alpha$  XRF data have the same intensity profile, which presents a rapid increase once the incidence angle exceeds the critical value, and reaches a maximum at  $\sim 0.265^\circ$ , indicating the presence of these elements in the same layer. In addition, the agreement between the best fit and the experimental results for the XRF data proves the reliability of the thicknesses, densities and elemental depth profiling in the layers.

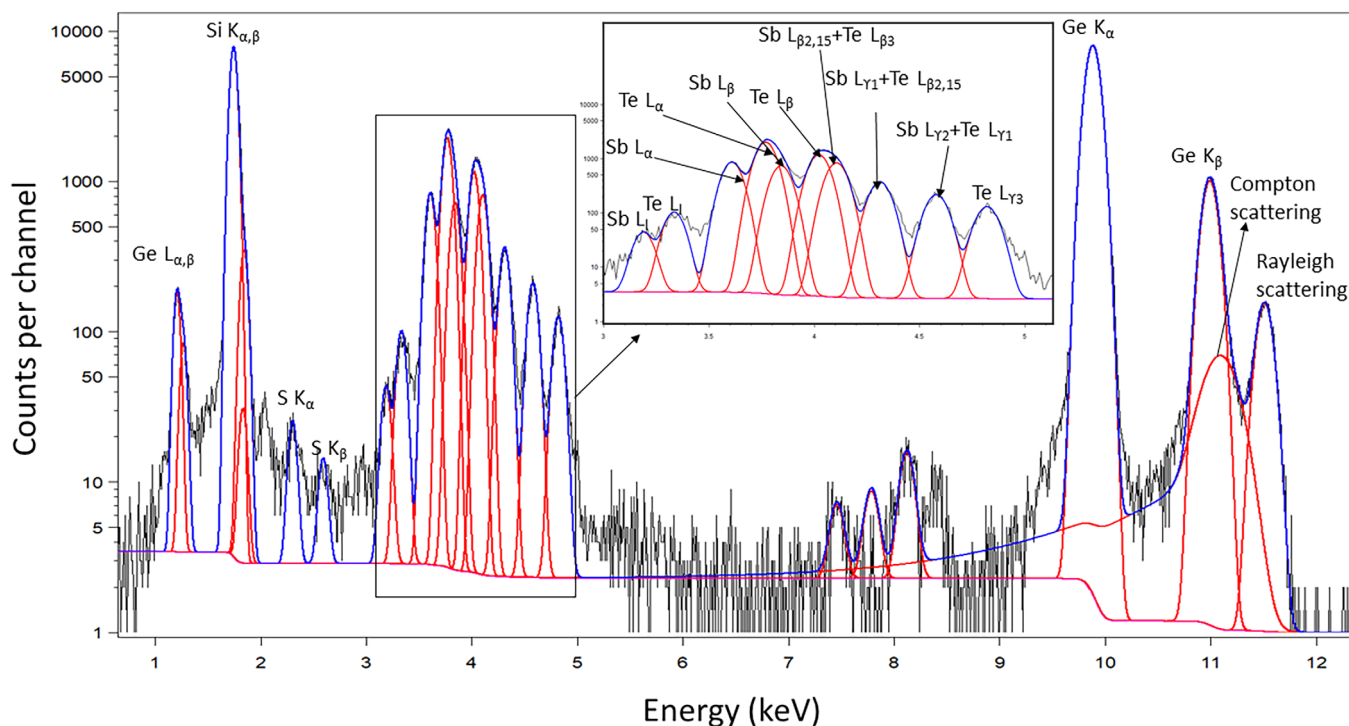


FIGURE 6 X-ray fluorescence spectrum measured and fitted at  $0.5^\circ$  using COLEGRAM.

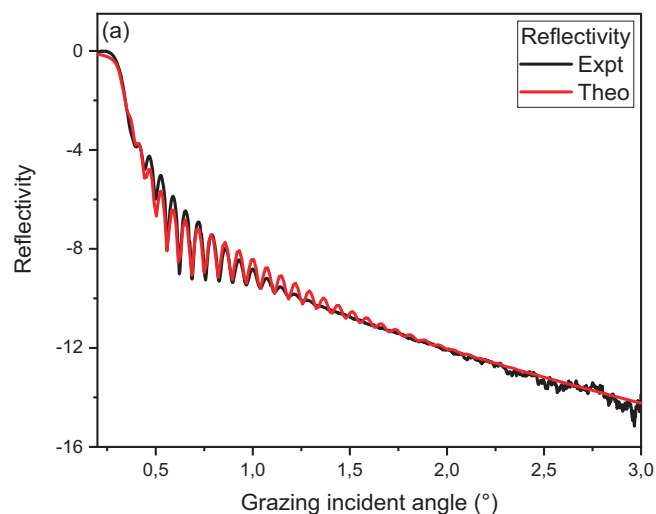


FIGURE 7 XRR intensity measured at 8 keV. The black and red curves represent the measured and the fitted reflectivity, respectively. XRR, X-ray reflectivity.

## 5.2 | Confidence interval of sample structure parameters

The structural parameters of the nominal structure C (3.5 nm)/Ge<sub>2</sub>Sb<sub>2</sub>Te<sub>5</sub> (50 nm)/Si substrate extracted from the best fitting with their associated confidence interval are presented in Table 2.

For the GST layer, we see a small difference between the nominal thickness of the GST layer (50 nm) and that

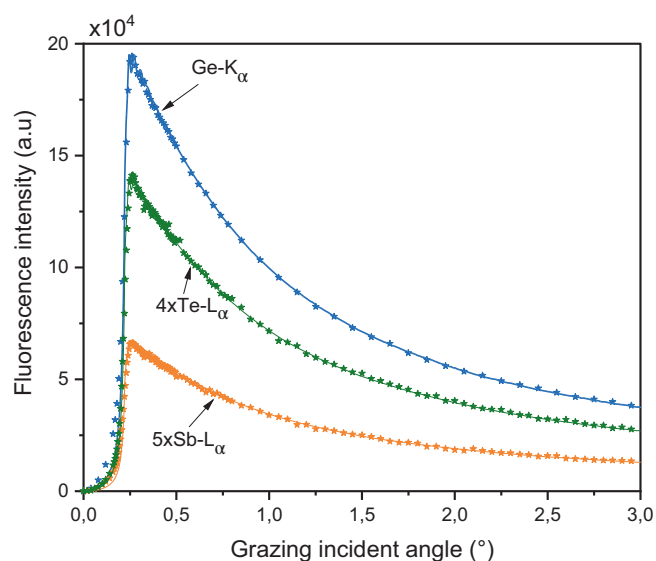


FIGURE 8 GIXRF of Ge-K $\alpha$  (blue), Sb-L $\alpha$  (orange), and Te-L $\alpha$  (green) measured at 11.5 keV. The stars represent the experimental data extracted with COLEGRAM for Ge-K $\alpha$ , Sb-L $\alpha$ , and Te-L $\alpha$ . The lines represent the fit to the data obtained with the ELIXIR in-house software. GIXRF, grazing incidence X-ray fluorescence.

of the best model (55 nm) that can be related to the uncertainty on the sample deposition method. However, it is important to note that a 10 % difference in thickness is relatively small and may not have a significant impact on the properties of the layer. In addition, we reported a

**TABLE 2** Layer parameters obtained from the best fitting of combined XRR-GIXRF on C (3.5 nm)/Ge<sub>2</sub>Sb<sub>2</sub>Te<sub>5</sub> (50 nm)/Si substrate with the bulk density of each layer.

Layer order	Composition	Thickness (nm)	Roughness(nm)	Density (g/cm <sup>3</sup> )	Nominal density (g/cm <sup>3</sup> )
1	C	3.50 ± 0.17	0.24 ± 0.01	2.30 ± 0.12	2.3
2	Ge <sub>1.8</sub> Sb <sub>2.2</sub> Te <sub>5</sub>	55.00 ± 1.11	2.00 ± 0.03	5.69 ± 0.09	5.88

density of 5.69 g/cm<sup>3</sup> for the GST layer, which is slightly lower than the bulk density of GST (5.88 g/cm<sup>3</sup>). The density difference of 3.2 % between the bulk and the calculated one could be due to the presence of voids or defects in the film, which could lower its overall density. The elemental composition of the GST layer was found to be Ge<sub>1.8</sub>Sb<sub>2.2</sub>Te<sub>5</sub> instead of the Ge<sub>2</sub>Sb<sub>2</sub>Te<sub>5</sub> given by the manufacturer. These differences could be due to variations in the manufacturing process. The capping layer is typically a thin and uniform layer that is used to protect the underlying layers from oxidation or contamination. As such, it is expected to be more stable during the deposition process compared to the GST layer. For this capping layer, we obtained a satisfactory result as the thickness and the density are identical to the nominal thickness and the bulk density respectively with a roughness lower than the thickness and lower than 2 nm. As a summary, despite small differences, the fitting procedure led to reasonable values of the elemental composition, roughnesses, and densities which are in good agreement with the nominal values.<sup>38,39</sup>

The confidence intervals of the model parameters were calculated by generating 100 Bootstrap samples using an enlargement factor of  $k = 1$ . This corresponds to a standard uncertainty with a 68.3 % confidence level. The application of the Bootstrap method on XRR-GIXRF data, presents relatively small confidence interval values on all the model parameters ( $\leq 5\%$ ). Therefore, the fitting procedure of combined XRR-GIXRF provides reliable structural parameters for thin film multilayers.

## 6 | CONCLUSION

GIXRF analysis was combined with XRR at the METROLOGIE beamline of the SOLEIL synchrotron and was applied to characterize a GST chalcogenide thin film. To validate the analysis method we have introduced a recursive method based on the Bootstrap technique to calculate the uncertainties on the model parameters obtained by the combined analysis. We also presented a Monte Carlo simulation method to calculate the uncertainty on the solid angle of detection taking into account the uncertainties of the geometrical parameters of the detector. Good agreement between the experimental and the

theoretical values was obtained, which validates the values of the optimized parameters. We have also seen that the reflectivity curve is affected by the geometrical factors as well as by the off-specular scattering. For the solid angle, low uncertainties were obtained, which makes their effects on the combined analysis negligible. Finally, the low values of the optimized parameter uncertainties calculated using the Bootstrap technique, have demonstrated that combined XRR-GIXRF analysis is a suitable method for thin film characterization.


## ACKNOWLEDGEMENTS

We acknowledge the SOLEIL synchrotron staff for smoothly running the facility. We are also grateful to Pascal Mercere and Paulo Da Silva for assistance in using the METROLOGIE beamline at the SOLEIL synchrotron.

## DATA AVAILABILITY STATEMENT

Research data are not shared.

## ORCID

Stephanie Melhem  <https://orcid.org/0000-0002-0439-8840>

Yves Ménesguen  <https://orcid.org/0000-0003-2505-979X>

## REFERENCES

- [1] A. V. Kolobov, P. Fons, A. I. Frenkel, A. L. Ankudinov, J. Tominaga, T. Uruga, *Nat. Mater.* **2004**, *3*, 703.
- [2] S. Raoux, M. Wuttig, *Phase Change Materials*, Springer, US, Boston, MA **2009**.
- [3] X. Sun, B. Yu, G. Ng, M. Meyyappan, *J. Phys. Chem. C* **2007**, *111*, 2421.
- [4] K. Kifune, Y. Kubota, T. Matsunaga, N. Yamada, *Acta Crystallogr. Sect. B: Struct. Sci.* **2005**, *61*, 492.
- [5] S. R. Ovshinsky, *Phys. Rev. Lett.* **1968**, *21*, 1450.
- [6] W. Pessoa, A. Roule, E. Nolot, Y. Mazel, M. Bernard, M.-C. Lépy, Y. Ménesguen, A. Novikova, P. Gergaud, F. Brigidi, *Spectrochim. Acta, Part B* **2018**, *149*, 143.
- [7] M. Wuttig, N. Yamada, *Nat. Mater.* **2007**, *6*, 824.
- [8] P. Hönicke, B. Detlefs, Y. Kayser, U. Mühle, B. Pollakowski, B. Beckhoff, *Journal of Vacuum Science & Technology A* **2019**, *37*, 041502. <https://doi.org/10.1116/1.5094891>
- [9] P. Hönicke, B. Detlefs, M. Müller, E. Darlatt, E. Nolot, H. Grampeix, B. Beckhoff, *Phys. Status Solidi A* **2015**, *212*, 523.
- [10] D. K. G. de Boer, *Phys. Rev. B* **1991**, *44*, 498.
- [11] D. Ingerle, M. Schiebl, C. Strel, P. Wobruschek, *Rev. Sci. Instrum.* **2014**, *85*, 83110.

- [12] A. J. Leenaers, J. Vrakking, D. K. de Boer, *Spectrochim. Acta, Part B* **1997**, *52*, 805.
- [13] O. Filies, O. Böling, K. Grewer, J. Lekki, M. Lekka, Z. Stachura, B. Cleff, *Appl. Surf. Sci.* **1999**, *141*, 357.
- [14] B. Beckhoff, R. Fliegau, M. Kolbe, M. Müller, J. Weser, G. Ulm, *Anal. Chem.* **2007**, *79*, 7873.
- [15] B. Beckhoff, *J. Anal. At. Spectrom.* **2008**, *23*, 845.
- [16] B. Beckhoff, A. Gottwald, R. Klein, M. Krumrey, R. Müller, M. Richter, F. Scholze, R. Thornagel, G. Ulm, *Phys. Status Solidi B* **2009**, *246*, 1415.
- [17] V. H. Elvira, M.-C. Lépy, Y. Ménesguen, *X-Ray Spectrom.* **2022**, *1*. <https://doi.org/10.1002/xrs.3318>
- [18] Y. Ménesguen, B. Boyer, H. Rotella, J. Lubeck, J. Weser, B. Beckhoff, D. Grötzsch, B. Kanngießer, A. Novikova, E. Nolot, M.-C. Lépy, *X-Ray Spectrom.* **2017**, *46*, 303.
- [19] BIPM, IEC, IFCC, ILAC, ISO, IUPAC, IUPAP, OIML, *JCGM* **2008**, *100*, 10. [https://www.bipm.org/documents/20126/2071204/JCGM\\_100\\_2008\\_E.pdf/cb0ef43f-baa5-11cf-3f85-4dcd86f77bd6](https://www.bipm.org/documents/20126/2071204/JCGM_100_2008_E.pdf/cb0ef43f-baa5-11cf-3f85-4dcd86f77bd6)
- [20] BIPM, IEC, IFCC, ILAC, ISO, IUPAC, IUPAP, OIML, *JCGM* **2008**, *101*, 24. [https://www.bipm.org/documents/20126/2071204/JCGM\\_101\\_2008\\_E.pdf/325dcaad-c15a-407c-1105-8b7f322d651c](https://www.bipm.org/documents/20126/2071204/JCGM_101_2008_E.pdf/325dcaad-c15a-407c-1105-8b7f322d651c)
- [21] P. R. G. Couto, J. C. Damasceno, S. P. Oliveira, *Theory and Applications of Monte Carlo Simulations*, Intechopen, Rijeka **2013**, p. 27. <https://doi.org/10.5772/53014>
- [22] E. Nolot, C. Sabbione, W. Pessoa, L. Prazakova, G. Navarro, *Appl. Surf. Sci.* **2021**, *536*, 147703.
- [23] C. Jeynes, E. Nolot, C. Costa, C. Sabbione, W. Pessoa, F. Pierre, A. Roule, G. Navarro, M. Mantler, *J. Anal. At. Spectrom.* **2020**, *35*, 701.
- [24] Y. Ménesguen, M.-C. Lépy, *X-Ray Spectrom.* **2011**, *40*, 411.
- [25] J. Lubeck, B. Beckhoff, R. Fliegau, I. Holfelder, P. Hönicke, M. Müller, B. Pollakowski, F. Reinhardt, J. Weser, *Rev. Sci. Instrum.* **2013**, *84*, 45106.
- [26] J. Lubeck, M. Bogovac, B. Boyer, B. Detlefs, D. Eichert, R. Fliegau, D. Grötzsch, I. Holfelder, P. Hönicke, W. Jark, R. B. Kaiser, B. Kanngießer, A. G. Karydas, J. J. Leani, M. C. Lépy, L. Lühl, Y. Ménesguen, A. Migliori, M. Müller, B. Pollakowski, M. Spanier, H. Sghaier, G. Ulm, J. Weser, B. Beckhoff, *AIP Conference Proceedings*, Vol. 1741, AIP Publishing LLC, New York **2016**, 30011.
- [27] D. L. Windt, *Comput. Phys.* **1998**, *12*, 360.
- [28] Y. Ménesguen, M.-C. Lépy, *Nucl. Instrum. Methods Phys. Res. Sec. A* **2021**, *1003*, 165341.
- [29] L. G. Parratt, *Phys. Rev.* **1954**, *95*, 359.
- [30] L. Nénot, P. Croce, *Revue de Physique Appliquée* **1980**, *15*, 761.
- [31] S. K. Ghose, B. N. Dev, *Phys. Rev. B* **2001**, *63*, 245409.
- [32] Y. Ménesguen, M.-C. Lépy, *Phys. Status Solidi A* **2022**, *219*, 2100423.
- [33] W. K. V. Chan, *Theory and applications of Monte Carlo simulations*, Intechopen, Rijeka **2013**.
- [34] B. Efron, R. J. Tibshirani, *An Introduction to the Bootstrap*, CRC press, New York **1994**.
- [35] K. Singh, M. Xie, *Bootstrap: A Statistical Method*, Rutgers University, USA **2008**, p. 1.
- [36] S. K. Sinha, *J. Phys. III* **1994**, *4*, 1543.
- [37] K. E. Torrance, E. M. Sparrow, *J. Opt. Soc. Am.* **1967**, *57*, 1105.
- [38] F. C. Mocanu, K. Konstantinou, T. H. Lee, N. Bernstein, V. L. Deringer, G. Csányi, S. R. Elliott, *J. Phys. Chem. B* **2018**, *122*, 8998.
- [39] M. Iwaki, *Surf. Coat. Technol.* **2002**, *158–159*, 377.

**How to cite this article:** S. Melhem, Y. Ménesguen, E. Nolot, M.-C. Lépy, *X-Ray Spectrom* **2023**, *1*. <https://doi.org/10.1002/xrs.3377>